Numerical Investigation of Oxygen Thermochemical Nonequilibrium on High-Enthalpy Double-Cone Flows

Jiaao Hao[a], Chih-Yung Wen[a,*]

[a] Department of Mechanical Engineering, The Hong Kong Polytechnic University, Kowloon,

Hong Kong

Abstract

Hypersonic thermochemical nonequilibrium flows over a double-cone configuration are numerically investigated. Simulations with oxygen as the test gas are performed using different coupling models of vibrational excitation and dissociation, including a conventional two-temperature model as the baseline and an improved model established on elementary kinetics and validated against existing shock tube experimental data. For the condition with the highest total enthalpy, the improved model predicts a larger separation region and greater peak heat flux with relative differences of 20.3% and 29.2%, respectively, compared with the baseline two-temperature model. The differences are attributed to inaccurate modeling of the vibration–dissociation coupling effects by the conventional two-temperature model, which overestimates the post-shock degree of dissociation and underestimates the post-shock temperature. The size of the separation bubble is therefore altered due to the change in its density. These findings may help to explain the large discrepancies found between numerical results and experimental data for high-enthalpy double-cone flows in hypersonic studies.

Keywords: hypersonic flow; thermochemical nonequilibrium; vibration–dissociation coupling; shock-wave/boundary-layer interaction

Nomenclature

e = specific total energy, J/kg

e_v = specific vibrational energy, J/kg

---

*Corresponding author
 Email address: cywen@polyu.edu.hk

F, G = vectors of inviscid fluxes in the x and y directions

F_v, G_v = vectors of viscous fluxes in the x and y directions

h_s = specific enthalpy of species s, J/kg

$J_{i,x}$ = mass diffusion flux of species i in the x direction, kg/m^2/s

$K_{eq,r}$ = equilibrium constant of reaction r, units in cgs

k_B = Boltzmann constant, 1.3807×10^{-23} J/K

$k_{f,r}$, $k_{b,r}$ = forward and backward reaction rate coefficient of reaction r, units in cgs

$k_{f,eq,r}$ = equilibrium forward reaction rate coefficient of reaction r, units in cgs

$k_{V-V-T}(i,j{\rightarrow}l,m)$, $k_{V-T}(i{\rightarrow}j)$ = forward rate coefficients for vibration–vibration–translation and vibration–translation transitions of molecular oxygen

$k_{V-D}(i{\rightarrow}c)$, $k_{V-D}(c{\rightarrow}i)$ = dissociation and recombination rate coefficients of molecular oxygen at the i-th vibrational quantum state, units in cgs

M_i = molecular mass of species i, g/mol

n_s = number density of species s, cm^{-3}

p = pressure, Pa

Q_v = vibrational partition function

$q_{tr,x}$ = translational–rotational heat flux in the x direction, J/m^2/s

$q_{v,x}$ = vibrational heat flux in the x direction, J/m^2/s

T_{tr} = translational–rotational temperature, K

T_{ve} = vibrational–electronic temperature, K

T_v = vibrational temperature, K

u, v = velocities in the x and y directions, m/s

Z = nonequilibrium factor

$\alpha_{r,i}$, $\beta_{r,i}$ = stoichiometric coefficients of reaction r

ε_i = vibrational energy of molecular oxygen at the i-th vibrational quantum state, J

$\theta_{v,s}$ = characteristic vibrational temperature of species s, K

$\theta_{d,s}$ = dissociation temperature of species s, K

ρ_i = density of species i, kg/m^3

ω_i = mass production rate of species i per unit volume, kg/m^3/s

ω_v = source term in vibrational energy equation, J/m^3/s

ω_{tv} = energy transport between the translational and vibrational modes, J/m^3/s

ω_{vd} = added or removed average vibrational energy due to recombination and dissociation, J/m^3/s

1 Introduction

Over the past several decades, hypersonic flight technology has attracted growing interest in both the military and non-military communities [1]. The continuous advances in hypersonic systems require a deep understanding of the flow characteristics over these vehicles. An important flow phenomenon that occurs in hypersonic flights is shock-wave/boundary-layer interaction (SWBLI), which can lead to a loss of control authority, peaks in surface heat transfer, and an adverse structural response induced by unsteadiness [2].

SWBLI can be effectively studied with various canonical configurations, including compression corners, shock impingement on flat plates, double wedges, and double cones. Among these models, the axisymmetric double-cone configuration is regarded as an important building block to understand SWBLI in hypersonic flows, which is able to sustain a strong interaction phenomenon, yet obviates the three-dimensional effects induced by the side walls in the two-dimensional counterparts [2,3].

Experimentally, hypersonic flow over a double cone has been systematically investigated at Calspan—University of Buffalo Research Center [4–9]. From 2001 to 2010, a series of double-cone experiments was conducted in the LENS I reflected shock tunnel with total enthalpies ranging from 3 to 15 MJ/kg in air, nitrogen, and oxygen. It was later found that the vibrational and chemical nonequilibrium in the freestream of the LENS I tunnel could have significant effects on the shock standoff distance and surface heating [8,10]. Therefore, in 2013, Holden et al. [9] conducted a new set of experiments in the LENS XX expansion tunnel, which provided a clean freestream environment without frozen vibrational energy and chemical compositions, with total enthalpies ranging from 5 to 22 MJ/kg in air.

The two sets of double-cone experiments have been widely used for computational fluid dynamics (CFD) code validation. Numerical simulations that correspond to the first set were presented by Candler et al. [11], Gaitonde et al. [12], Nompelis et al. [13], Druguet et al. [14,15], and Knight et al. [16]. These studies found that good agreement with experimental measurements could be obtained for the nitrogen flow cases without obvious dissociation, whereas large discrepancies were observed for the air and oxygen flows in the presence of thermochemical nonequilibrium. It was therefore suspected that the vibrational and chemical nonequilibrium in the freestream of the LENS I tunnel and the inaccurate modeling of oxygen vibrational excitation and dissociation could be responsible for the discrepancies [9]. However, although a clean freestream was provided in the LENS XX tunnel, discrepancies were still found between CFD results and the experimental data [17]. A more recent study [18] numerically simulated the double-cone flows under conditions corresponding to the recent experiments using two different vibration–dissociation coupling models, including the popular Park model [19] and the coupled vibration-dissociation-vibration (CVDV) model [20]. It was found that the difference between the results from the Park and CVDV models increased with the total enthalpy. Although the CVDV model predicted closer agreement with the experimental data, but the sizes of the separation regions were still significantly underestimated. It was suggested that state-specific simulations should be performed

to exclude the inherent defect of the current vibration–dissociation coupling models. However, tracing the temporal and spatial variation of each vibrational level would require considerable computational resources. Consequently, detailed state-specific simulations have been applied only to one- and two-dimensional inviscid flows [21,22]. Calculations of complex viscous flows such as those around a double-cone configuration using the state-specific method with detailed elementary processes have yet to be made.

It is therefore the objective of this study to develop a computationally affordable model for the process of oxygen vibrational excitation and dissociation and to investigate its effects on high-enthalpy double-cone flows in comparison with a conventional two-temperature model. Efforts are devoted to reveal the cause of the great discrepancies found between numerical results and experimental data for such flows. An oxygen vibration–dissociation coupling model is firstly established based on the kinetic rates for elementary processes and validated against existing shock tube experimental data. High-enthalpy double-cone flows are then simulated with the baseline and improved models. Finally, the conclusions are summarized.

2 Governing equations and numerical methods

Under the two-temperature assumption, the translational–rotational energy mode is considered to be fully excited in terms of a translational–rotational temperature T_{tr}, and the vibrational energy of molecules and the electronic excitation energy are in equilibrium corresponding to a vibrational–electronic temperature T_{ve}. Because only the ground electronic energy level is considered for the species involved in this investigation, T_{ve} is reduced to a vibrational temperature T_v. For axisymmetric flows, the conservation equations of species mass, mixture momentum, total energy, and vibrational energy can be written as follows:

$$\frac{\partial}{\partial t}\int_{\Omega} U d\Omega + \oint_{\partial\Omega}\left[\left(\boldsymbol{F}-\boldsymbol{F}_v\right)n_x+\left(\boldsymbol{G}-\boldsymbol{G}_v\right)n_y\right]y dS = \int_{\Omega}\left(\boldsymbol{S}+\boldsymbol{S}_{axis}\right)d\Omega,\tag{1}$$

where x and y are the coordinates in the axial and radial directions, respectively. The vectors of the conservative variables and source terms are given by

$$U = \begin{pmatrix} \rho_i \\ \rho u \\ \rho v \\ \rho e \\ \rho e_v \end{pmatrix}, \quad S = \begin{pmatrix} \omega_i \\ 0 \\ 0 \\ 0 \\ \omega_v \end{pmatrix}, \quad S_{axis} = \frac{1}{y}\begin{pmatrix} 0 \\ 0 \\ p - \tau_{yy} \\ 0 \\ 0 \end{pmatrix}, \tag{2}$$

where ρ_i is the density of species i, ρ is the density of the mixture, u and v are the velocities in the axial and radial directions, respectively, p is the pressure, e is the specific total energy of the mixture, e_v is the specific vibrational energy of the mixture, and ω_i and ω_v represent the production rates of species mass and vibrational energy per unit volume, respectively.

The vectors of inviscid and viscous fluxes in the axial direction are expressed as

$$F = \begin{pmatrix} \rho_i u \\ \rho u^2 + p \\ \rho uv \\ (\rho e + p)u \\ \rho e_v u \end{pmatrix}, \quad F_v = \begin{pmatrix} -J_{i,x} \\ \tau_{xx} \\ \tau_{xy} \\ u\tau_{xx} + v\tau_{xy} - (q_{tr,x} + q_{v,x}) - \sum_{s=1}^{ns} J_{s,x} h_s \\ -q_{v,x} - \sum_{s=mol.} J_{s,x} e_{v,s} \end{pmatrix}, \tag{2}$$

where ns denotes the total number of species, mol. denotes the molecule species, h_s and $e_{v,s}$ are the specific enthalpy and vibrational energy of species s, respectively, $J_{i,x}$ is the mass diffusion flux of species i in the axial direction, and $q_{tr,x}$ and $q_{v,x}$ are the translational–rotational and vibrational heat fluxes in the axial direction, respectively. The flux vectors in the radial directions are similar.

According to the law of mass reaction, ω_i can be obtained by

$$\omega_i = M_i \sum_{r=1}^{nr} (\beta_{r,i} - \alpha_{r,i})\left(k_{f,r} \prod_{j=1}^{ns} \left(\frac{\rho_j}{M_j}\right)^{\alpha_{r,i}} - k_{b,r} \prod_{j=1}^{ns} \left(\frac{\rho_j}{M_j}\right)^{\beta_{r,i}} \right), \tag{4}$$

where nr denotes the total number of reactions, M_i is the molecular mass of species i, and $\alpha_{r,i}$ and $\beta_{r,i}$ are the stoichiometric coefficients of reaction r. $k_{f,r}$ and $k_{b,r}$ are the forward and backward rate coefficients of reaction r, respectively, which can be expressed as

$$k_{f,r} = Z k_{f,eq,r}, \quad k_{b,r} = \frac{k_{f,eq,r}}{K_{eq,r}}. \tag{5}$$

In these expressions, Z is the nonequilibrium factor, and $k_{f,eq,r}$ and $K_{eq,r}$ are the

equilibrium forward rate coefficient and the equilibrium constant of reaction r, respectively.

ω_v can be further decomposed into two parts as

$$\omega_v = \omega_{tv} + \omega_{vd},\qquad(6)$$

where ω_{tv} represents the energy transfer between the translational mode of heavy particles and the vibrational mode of molecules, and ω_{vd} accounts for the added or removed vibrational energy induced by recombination and dissociation. Modeling of these two terms is discussed in the next section.

The viscous stresses are modeled assuming a Newtonian fluid under Stokes' hypothesis. Heat fluxes are calculated according to Fourier's law for all energy modes. The species mass diffusion fluxes are modeled using the modified Fick's law to ensure that the sum of the diffusion fluxes is zero [23]. The transport properties of the gas mixture are calculated using Gupta's mixing rule [24] with the collision integrals data provided by Wright et al. [25].

The numerical simulations in this study are performed using a multiblock parallel finite-volume CFD code called PHAROS [26,27]. The inviscid terms are evaluated using the modified Steger–Warming scheme [28], which is able to capture strong shocks stably while maintaining sufficient viscous resolution. The fluxes are then extended to higher orders by monotone upstream-centered schemes for conservation laws (MUSCL) reconstruction [29] with the van Leer slope limiter [30]. The viscous fluxes are calculated using a second-order central difference. A line relaxation method [31] is used for time marching.

3 Modeling of oxygen vibrational excitation and dissociation

3.1 Baseline model

The baseline model uses Park's 1990 chemical reaction model [19] to calculate the equilibrium rate coefficients. ω_{tv} is modeled using the Landau–Teller model [32], in which the vibrational relaxation times are calculated via the Millikan–White expression [33] with the parameters given by Hash et al. [34]. Park's correction [19] is introduced to avoid underprediction of the relaxation times at high temperatures. The

CVDV model [20] is used to account for the vibration–dissociation coupling effects, which assumes that truncated harmonic oscillators relax via Boltzmann distributions corresponding to T_v and that the probabilities of dissociation scale exponentially with the vibrational levels. The resulting nonequilibrium factor Z_{baseline} can be evaluated from

$$Z_{\text{baseline}} = \frac{Q_v(T_{\text{tr}})Q_v(T_F)}{Q_v(T_v)Q_v(-U)}, \tag{7}$$

where Q_v is the vibrational partition function and T_F is defined by

$$\frac{1}{T_F} = \frac{1}{T_v} - \frac{1}{T_{\text{tr}}} - \frac{1}{U} \tag{8}$$

with U as a parameter in unit of temperature.

ω_{vd} can be obtained by

$$\omega_{\text{vd}} = \omega_b E(-U) - \omega_f E(T_F). \tag{9}$$

In the expression, ω_f and ω_b are the forward and backward rates of the molecular number density production per unit volume, respectively. The function of the weighted average vibrational energy is defined by

$$E(T) = \frac{k_B \theta_{v,s}}{\exp(\theta_{v,s}/T) - 1} - \frac{k_B \theta_{d,s}}{\exp(\theta_{d,s}/T) - 1}, \tag{10}$$
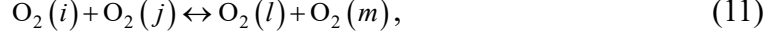
where k_B represents the Boltzmann constant, and $\theta_{v,s}$ and $\theta_{d,s}$ denote the characteristic vibrational temperature and the dissociation temperature of species s, respectively. Based on a comparison with the state-specific data obtained using the forced harmonic oscillator (FHO) model and the quasi-classical trajectory (QCT) method, the semi-empirical parameter U is set to be one third of the species dissociation temperature for O_2, as recommended by Hao et al. [35].

3.2 Improved model

In this section, an improved model is established using the elementary kinetic rate coefficients to express ω_{tv} and ω_{vd} under the two-temperature assumption, which acknowledges that the vibrational level distribution can be described by the Boltzmann distribution in terms of a single vibrational temperature. The improved model therefore represents the upper performance limit of a two-temperature model.

Vibration–vibration–translation (V–V–T) bound–bound transitions induced by O_2 impacts, vibration–translation (V–T) bound–bound transitions induced by O impacts, and vibration–dissociation (V–D) bound–free transitions are considered and expressed as follows:

$$O_2(i) + O_2(j) \leftrightarrow O_2(l) + O_2(m), \tag{11}$$

$$O_2(i) + O \leftrightarrow O_2(j) + O, \tag{12}$$

$$O_2(i) + M \leftrightarrow O + O + M, \tag{13}$$

where i, j, l, and m represent the vibrational quantum numbers of O_2, and M stands for the third particle. With the V–V–T and V–T transitions taken into account, ω_{tv} can be readily obtained by

$$
\begin{aligned}
\omega_{tv} = &\sum_i \varepsilon_i \sum_j \sum_l \sum_m k_{V-V-T}(l,m \to i,j) n_{O_2(l)} n_{O_2(m)} \\
&- \sum_i \varepsilon_i \sum_j \sum_l \sum_m k_{V-V-T}(i,j \to l,m) n_{O_2(i)} n_{O_2(j)} \\
&+ \sum_i \varepsilon_i \sum_j \left\{ k_{V-T}(j \to i) n_{O_2(j)} n_O - k_{V-T}(i \to j) n_{O_2(i)} n_O \right\}
\end{aligned}
\tag{14}
$$

where ε_i is the vibrational energy of the i-th vibrational quantum state, n is the species number density, and $k_{V-V-T}(i,j{\to}l,m)$ and $k_{V-T}(i{\to}j)$ are the forward rate coefficients of V–V–T and V–T transitions, respectively.

Based on Eq. (13), the production rate of $O_2(i)$ can be expressed as

$$\frac{d}{dt} n_{O_2(i)} = k_{V-D}^M(c \to i) n_O n_O n_M - k_{V-D}^M(i \to c) n_{O_2(i)} n_M, \tag{15}$$

where $k_{V-D}(i{\to}c)$ and $k_{V-D}(c{\to}i)$ are the rate coefficients of dissociation and recombination, respectively, with superscripts representing the collision partners. With the vibrational levels summed up, the total production rate of O_2 is given by

$$\frac{d}{dt} n_{O_2} = k_{V-D,b}^M n_O n_O n_M - k_{V-D,f}^M n_{O_2} n_M, \tag{16}$$

where the total dissociation and recombination rate coefficients, $k_{V-D,f}$ and $k_{V-D,b}$, are defined by

$$k_{V-D,f}^M = \sum_i k_{V-D}^M(i \to c) \frac{n_{O_2(i)}}{n_{O_2}}, \tag{17}$$

$$k_{V-D,b}^{M} = \sum_{i} k_{V-D}^{M}(c \to i). \tag{18}$$

Under equilibrium conditions, the total dissociation rate coefficient can be evaluated from

$$k_{V-D,f,eq}^{M} = \sum_{i} k_{V-D}^{M}(i \to c) \frac{\exp(-\varepsilon_i/k_B T_{tr})}{Q_v(T_{tr})}. \tag{19}$$

The nonequilibrium factor $Z_{improved}$ can therefore be obtained by

$$Z_{improved} = \frac{k_{V-D,f}^{M}}{k_{V-D,f,eq}^{M}}. \tag{20}$$

Furthermore, ω_{vd} can be written as

$$\omega_{vd} = \omega_b E_b - \omega_f E_f, \tag{21}$$

where the terms that represent the forward and backward weighted average vibrational energy, E_f and E_b, are given by

$$E_f = \sum_{i} \varepsilon_i \frac{k_{V-D}^{M}(i \to c)}{k_{V-D,f}^{M}} \frac{n_{O_2(i)}}{n_{O_2}}, \tag{22}$$

$$E_b = \sum_{i} \varepsilon_i \frac{k_{V-D}^{M}(c \to i)}{k_{V-D,b}^{M}}. \tag{23}$$

In the improved model, 47 vibrational levels given by Andrienko and Boyd [36] are considered for molecular oxygen in the ground electronic state. The O_2–O_2 V–V–T transition rate coefficients are generated using the FHO model [21]. According to the state-specific results of Hao et al. [21], the multi-quantum V–V–T transitions with jumps larger than 5 are neglected to reduce the computation burden. The O_2–O_2 V–D rate coefficients are taken from the FHO analysis of Lino da Silva et al. [37], and the O_2–O V–T and V–D rate coefficients are taken from the QCT calculations of Andrienko et al. [38,39]. The rate coefficients of the forward and backward processes can be correlated using the principle of detailed balance.

4 Validation: post-shock flows

In this section, thermochemical nonequilibrium flows of oxygen behind a normal shock under conditions corresponding to the experiments of Ibraguimova et al. [40] are investigated to validate the established model.

4.1 Flow conditions

Ibraguimova et al. [40] determined the vibrational temperature profiles of oxygen behind the front of shock waves in a shock tube with the translational temperature immediately across the shock ranging from 4000 to 10,800 K. The stationary test gas in the low-pressure chamber ahead of the shock waves was pure oxygen. Table 1 summarizes the three experimental flow conditions considered in this investigation, where V_s represents the velocity of the shock wave and p_1 and T_1 are the pressure and the temperature, respectively, ahead of the shock front. The post-shock distributions of the translational–rotational temperature and the concentration of atomic oxygen were also evaluated by solving the gas dynamics equations with the measured vibrational temperatures. With the increase in the post-shock translational temperature and the decrease in the pressure, the process of vibrational excitation and dissociation becomes increasingly intense from cases 1 to 3.

Table 1. Flow conditions for shock-tube experiments [40].

Case no.	V_s (m/s)	p_1 (Pa)	T_1 (K)
1	3070	266.644	295
2	3950	133.322	295
3	4440	106.658	295

In the shock reference frame, the governing equations in Section 2 can be simplified into the one-dimensional inviscid compressible flow equations, which can be easily solved with the space marching method. The initial condition is derived from the Rankine–Hugoniot relations assuming the frozen vibrational mode and chemical composition. An explicit fourth-order Runge–Kutta scheme is used for numerical integration.

4.2 Comparison with experiments

Figure 1 presents the post-shock profiles of T_{tr} and T_v calculated with the baseline and improved models for the three cases as a function of t defined by $t = x/V_s$, where x is the distance from the shock. It also shows the state-specific results from Hao et al. [21] and the experimental data of T_{tr} and T_v. Note that the data of T_{tr} are not available for case 1. Hao et al. [21] were among the first to fully simulate the process of oxygen vibrational excitation and dissociation using the state-specific method with detailed

elementary kinetics. Their study can therefore be regarded as a reliable reference. Because multiple definitions of T_v have been given for state-specific simulations, only the post-shock profiles of T_{tr} are shown here.

For case 1, the improved model predicts a shorter vibrational relaxation time than the baseline model, but both distributions of T_v calculated with the two models could fall within the uncertainty of the experimental data. For cases 2 and 3, the baseline and improved models both fail to reproduce the measurements of T_v. In fact, the shock-tube data of T_v were determined based on the oxygen absorbance in Schumann–Runge bands, hence a global vibrational temperature defined under the two-temperature assumption is inadequate. Nevertheless, the improved model predicts a higher post-shock T_{tr} than the baseline model, which shows better agreement with the state-specific results and the experimental data.

Figure 2 shows the post-shock mass fraction profiles of atomic O predicted by different models for case 3. The degree of dissociation predicted by the improved model is much lower than that obtained by the baseline model, which again shows better agreement with the reference results.

In general, the improved model could yield more accurate predictions of post-shock properties than the conventional two-temperature model. However, there is still room for improvement relative to the state-specific method under conditions similar to those of cases 2 and 3, in which the non-Boltzmann distribution effects could be significant.

(a) Case 1   (b) Case 2
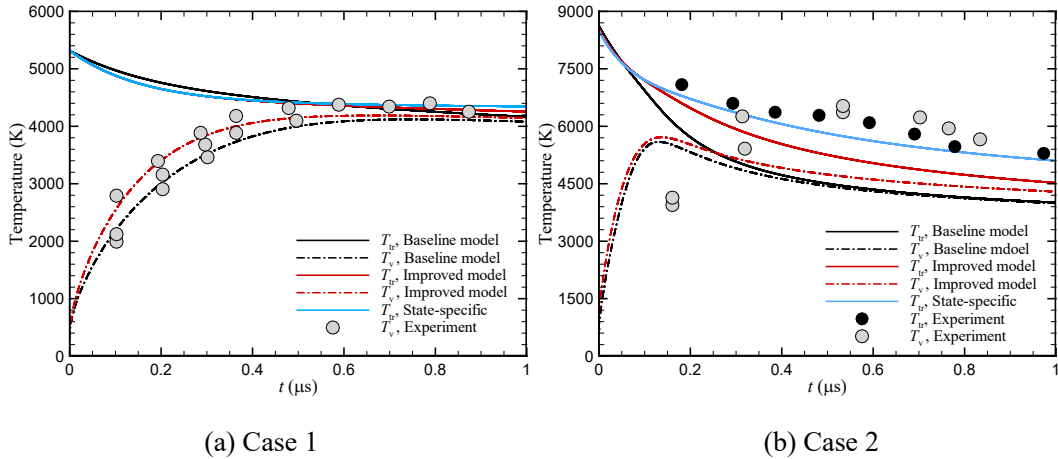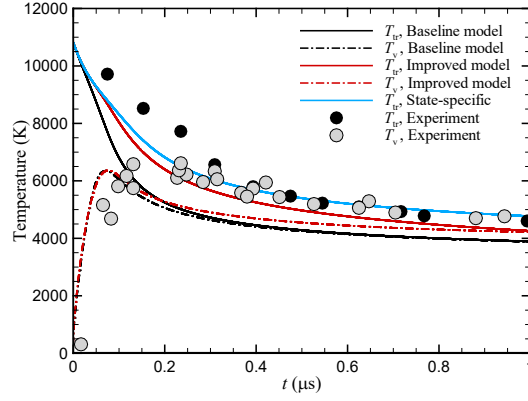
(c) Case 3

Fig. 1. Post-shock temperature profiles predicted by different models.
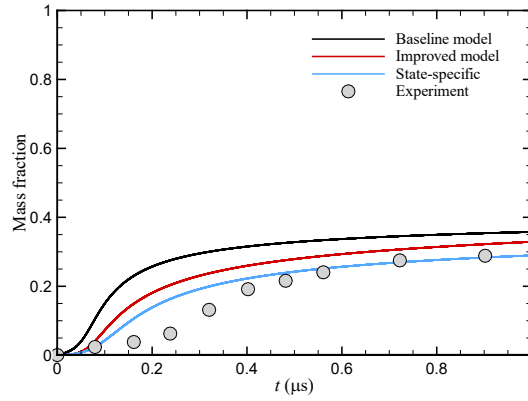
**Fig. 2. Post-shock mass fraction profiles of atomic O predicted by different models for case 3 in Table 1.**

5 Results: double-cone flows

Given the improved model's substantial improvement of post-shock distribution predictions, it is of interest to investigate whether the improved model would generate more accurate predictions on high-enthalpy double-cone flows. In this section, thermochemical nonequilibrium flows around a double-cone configuration are simulated using different models of vibrational excitation and dissociation.

5.1 Geometric configuration and flow conditions

The double-cone geometry, as illustrated in Fig. 3, has two conical sections of half-angles of 25° and 55°, and the surfaces are each 10.16 cm long. The geometric configuration replicates the experimental models in Nompelis et al. [7] and Holden et al. [8] and remains identical for all flow conditions involved in this study. Figure 3 also shows the coordinate system, with the origin located at the nose of the first cone

13

and the horizontal axis coinciding with the cone axis.
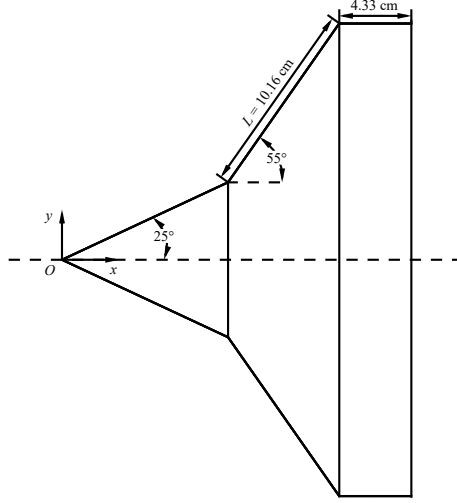
Fig. 3. Double-cone geometry.

Three flow conditions are considered and listed in Table 2. V_∞, $T_{tr,\infty}$, $T_{v,\infty}$, and ρ_∞ are the freestream velocity, translational–rotational temperature, vibrational temperature, and density, respectively, h_0 is the specific total enthalpy, and Y is the species mass fraction. All of the flows are assumed to be laminar due to the relatively low Reynolds numbers. Runs 88 and 91 were conducted in the LENS I tunnel, hence a certain level of thermochemical nonequilibrium was present in the freestream. To be precise, the nozzle flow should be simulated by the state-specific method to provide a more accurate freestream condition. Instead, given that the information on the nozzle shape is unavailable, the flow conditions used in this study are taken from the results of the two-temperature nozzle simulations in Nompelis et al. [7], which may introduce some errors. In addition to runs 88 and 91, run 4 conducted in the LENS XX tunnel is selected as a test case in this study because it has the highest total enthalpy and the difference between the Park and CVDV models in the length of the separation region is the largest as documented by Hao et al. [18]. For run 4, the test gas is replaced by pure oxygen in a thermochemical equilibrium state, and thus no direct comparison with the experimental data is made.

Table 2. Freestream conditions for double-cone experiments [7,8].

Run no.	V_∞ (m/s)	$T_{tr,\infty}$ (K)	$T_{v,\infty}$ (K)	ρ_∞ (g/m^3)	h_0 (MJ/kg)	Y_{O2}	Y_O
88	3246	569.8	697.6	1.0613	8.78	0.9482	0.0518
91	4303	729.0	773.1	1.5498	10.26	0.9389	0.0611

| 4 | 6497 | 652.0 | 652.0 | 0.9640 | 21.77 | 1.0000 | 0.0000 |

5.2 Grid independence

It is well known that prediction of shock interaction and separated flow is very sensitive to the level of numerical dissipation, especially the choice of numerical schemes and grid resolution. According to Druguet et al. [41], the modified Steger–Warming scheme and the van Leer limiter used in this study should be adequate for the requirement of numerical dissipation.

To determine the required grid resolution, a grid independence study is performed for run 4 (the case with the highest enthalpy) using the baseline model with three levels of grid refinement: 512×256 (coarse), 1024×512 (medium), and 2048×1024 (fine). For all of the grids, the normal spacing at the double-cone surface is set to 1×10^{-7} m to ensure that the grid Reynolds number is on the order of magnitude of one. In addition, the surface is assumed to be noncatalytic, with a fixed wall temperature of 300 K.

Figure 4 compares the predicted distributions of surface pressure, heat flux, and skin friction among the three grids for run 4. Note that the region of the interaction has been enlarged. Flow separation and reattachment occur at the locations where skin friction equals zero. The separation region can also be indicated by the sudden change in surface pressure and heat flux. It is observed that the separation zone increases and converges on a certain level as the grid refines. The medium grid (1024×512) is considered to be adequate to ensure grid independence because the distributions obtained using the medium and fine grids almost overlap.
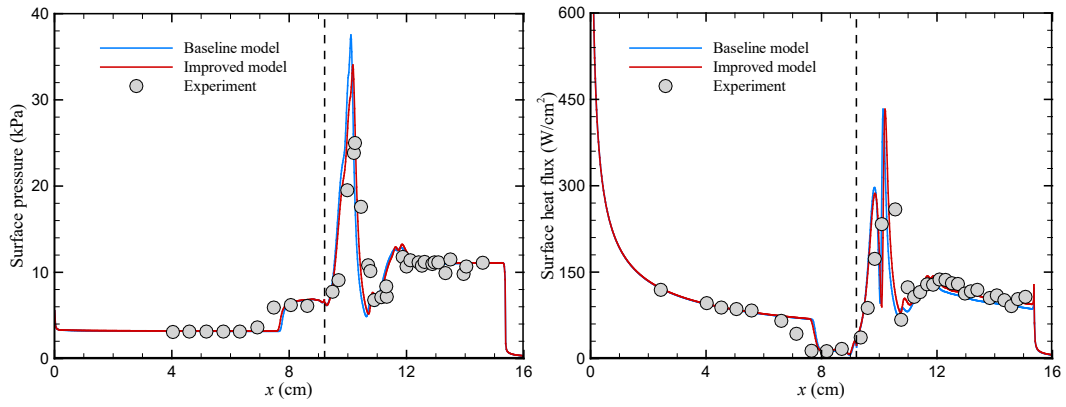

(a) Surface pressure   (b) Surface heat flux
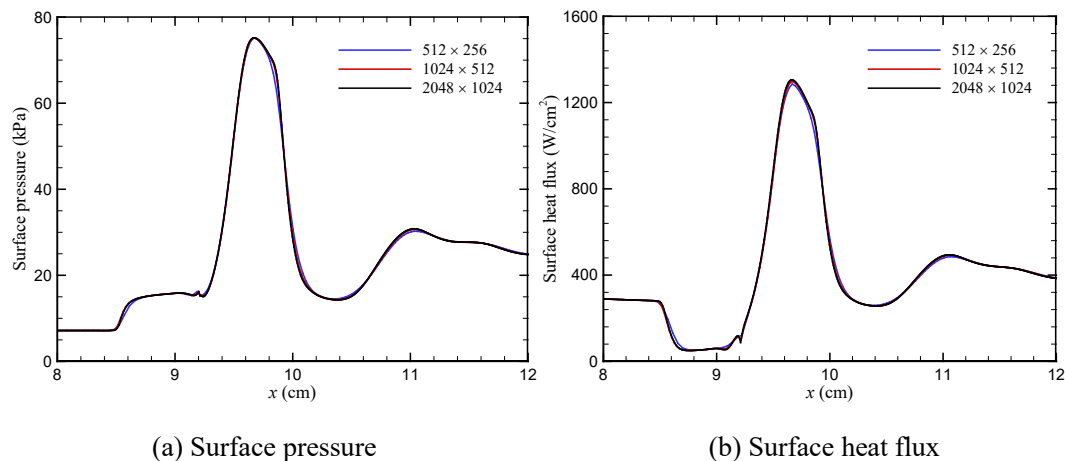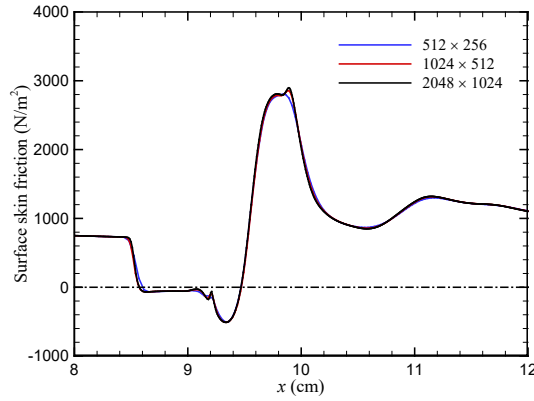
(c) Surface skin friction

Fig. 4. Grid sensitivity for run 4.

**5.3 Effects of vibration excitation and dissociation models**

Figure 5 presents the distributions of surface pressure and heat transfer predicted by the baseline and improved models for the three flow conditions together with the experimental data. The two models predict similar results for runs 88 and 91 due to the relatively low total enthalpies. The agreement with the measurements is generally good, especially for run 91. For run 88, the CFD results tend to underestimate the size of the separation region, which could be attributed to the abovementioned inaccuracy of the freestream condition. For run 4, more accurate modeling of oxygen vibrational excitation and dissociation leads to a relatively larger separation region. The size of the separation region, defined as the axial distance between the separation point on the first cone and the reattachment point on the second cone, increases by 20.3% (see Fig. 6). However, the locations of the peak pressure and heat flux do not change substantially. There is no significant difference in the surface pressure in the region of the interaction, but a greater surface heat transfer is predicted by the improved model than by the baseline model for nearly the entire second cone, with the peak heat flux increasing by 29.2%.
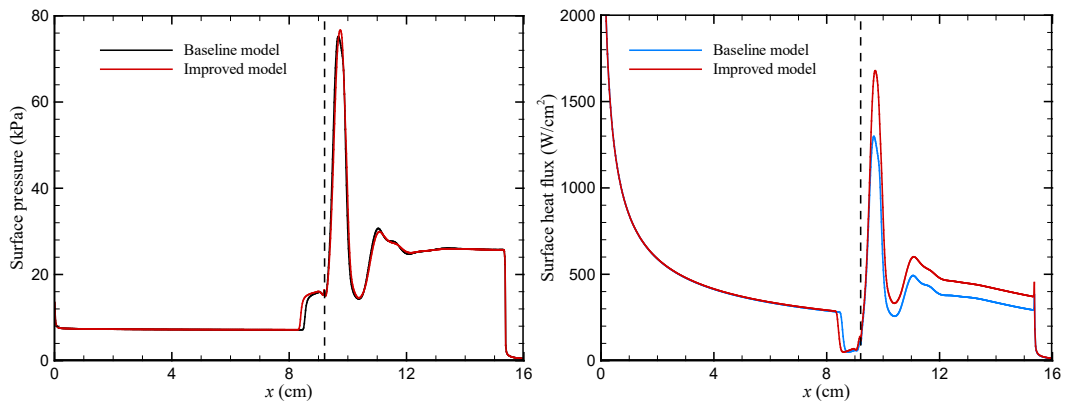
(a) Surface pressure for run 88

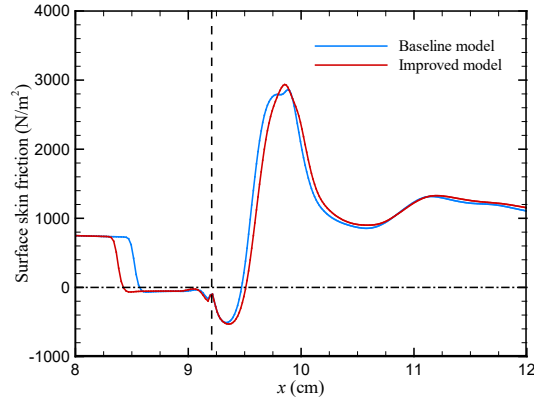(b) Surface heat transfer for run 88
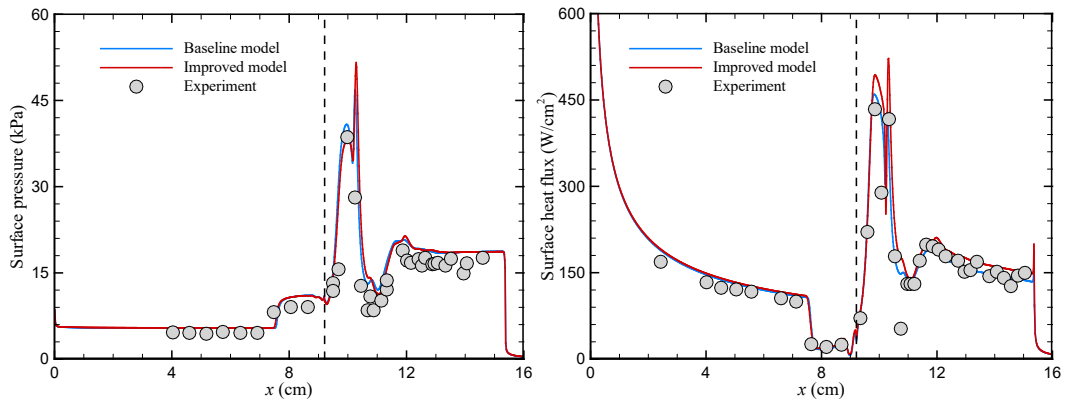
(c) Surface pressure for run 91

(d) Surface heat transfer for run 91

(e) Surface pressure for run 4

(f) Surface heat transfer for run 4

Fig. 5. Comparison of surface pressure and heat flux. Dashed line demarcates the hinge of the forward and aft cones.

Fig. 6. Comparison of surface skin friction for run 4. Dashed line demarcates the hinge of the forward and aft cones.

To further investigate the physics behind the observed difference, the flowfields obtained for run 4 are further examined. Figure 7 illustrates the contours of the density gradient magnitude predicted by the baseline and improved models. An attached shock (AS) wave is produced by the first cone, whereas a detached shock (DS) is induced by the second cone. Due to the presence of a large-scale flow separation region, a separation shock (SS) is formed that alters the strength and inclination of the attached shock. The separation shock further intersects with the reattachment shock (RS) at the triple point (TP). These flow features resemble Edney's type VI shock interaction [42], which is characterized by a centered expansion and a slip line (SL) emanating from the triple point. The interaction structures obtained by the two models are similar except that the separation region is larger, and the detached shock lies farther from the cone surface when the improved model is used.
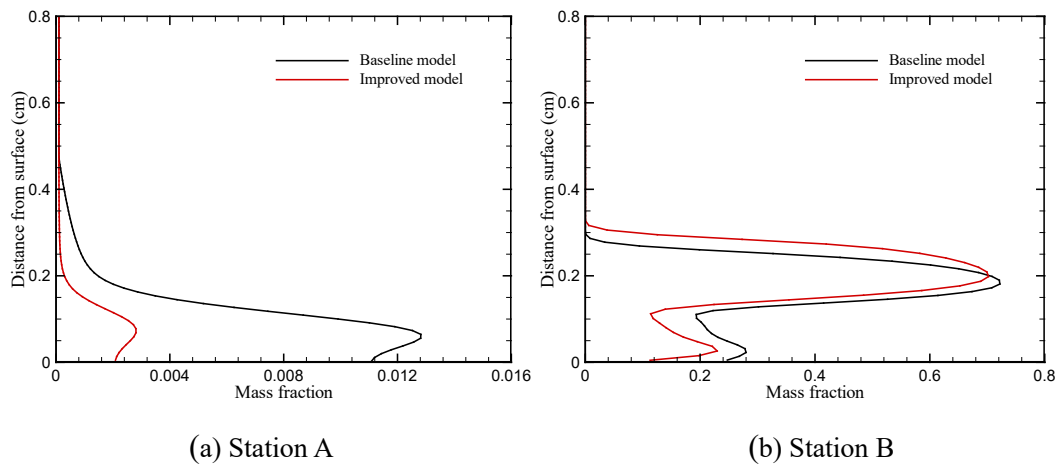
(a) Baseline model   (b) Improved model
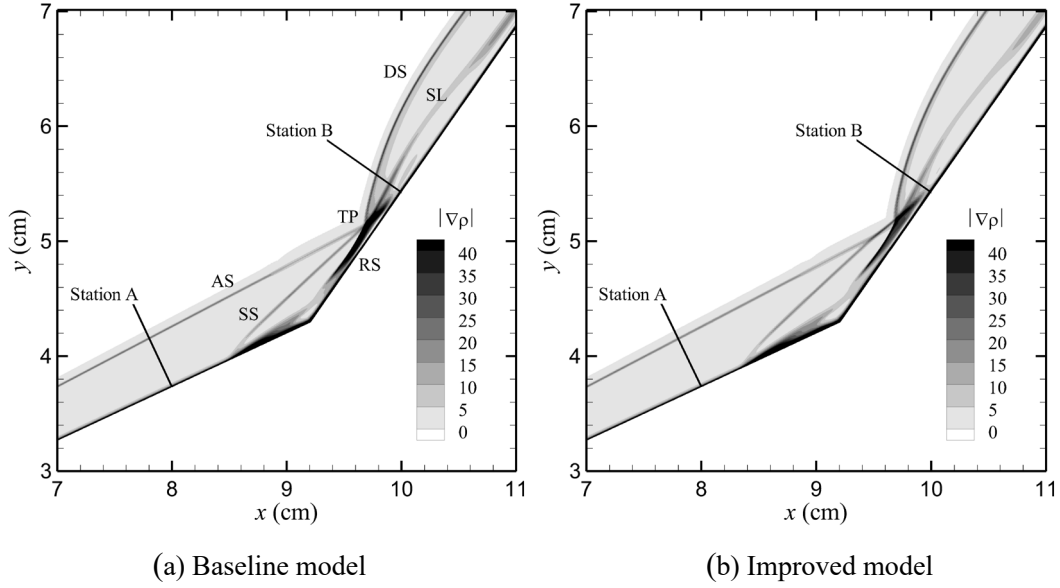
Fig. 7. Contours of density gradient magnitude predicted by the baseline and improved models for run 4.

The wall-normal distributions of flow quantities are extracted at two stations: A and B. Station A is located on the surface of the first cone and is upstream of the separation point ($x = 8$ cm), whereas station B is positioned on the second cone near the reattachment point behind the detached shock ($x = 10$ cm). Figures 8 and 9 show the distributions of temperatures and mass fractions of atomic O predicted by the baseline and improved models as a function of the normal distance from the wall at the two stations. At station A, the temperature profiles are nearly identical for both models. T_{tr} experiences a sudden increase from the attached shock, whereas the increase of T_v turns out to be much milder. The second peak of T_{tr} near the surface is caused by viscous dissipation. Although the mass fraction distributions of atomic O show remarkable differences between the two models, the degree of dissociation is too low to affect the flow quantities. As expected, the attached shock is unaffected by the models of vibrational excitation and dissociation, as shown in Fig. 7. At station B, the improved model predicts a lower degree of dissociation behind the detached shock than the baseline model, similar to that observed in Section 4.2, due to an increase in the post-shock T_{tr}. Consequently, the post-shock density decreases (see Fig. 10), and the shock standoff distance, defined as the normal distance between the location of the peak T_{tr} and the surface, increases when the improved model is used. In addition, the

greater heat flux on the second cone predicted by the improved model is caused by the

larger temperature gradient near the surface, as seen in Fig. 8.

(a) Station A   (b) Station B
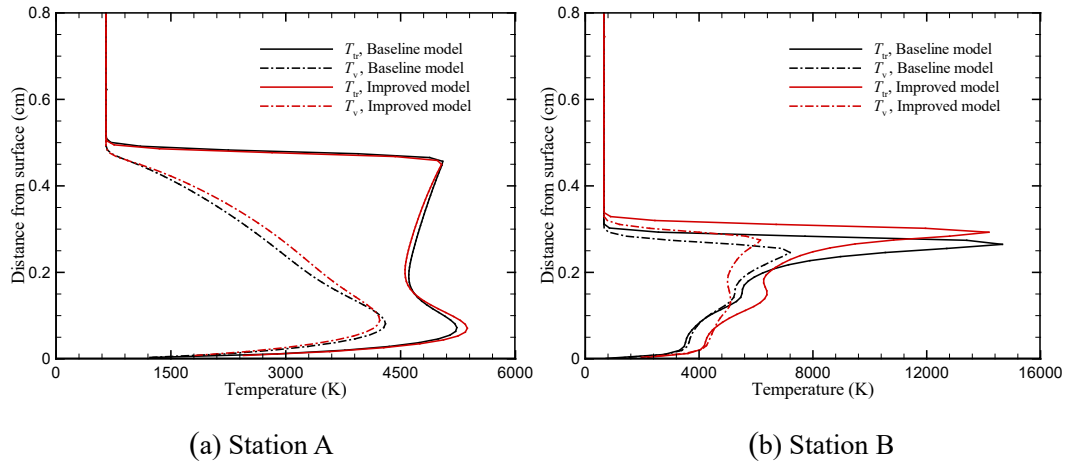
Fig. 8. Surface-normal temperature distributions predicted by the baseline and improved

models at stations A and B in Fig. 7 for run 4.


(a) Station A   (b) Station B

Fig. 9. Surface-normal mass fraction distributions of atomic O predicted by the baseline and

improved models at stations A and B in Fig. 7 for run 4.
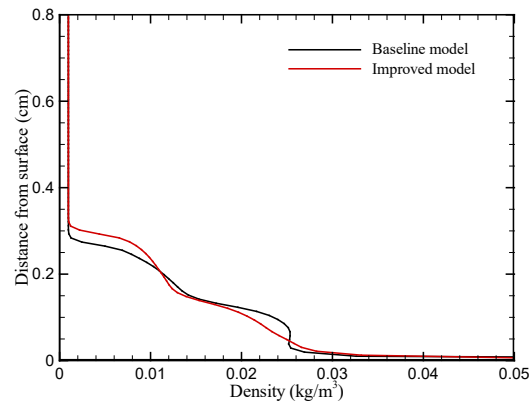
Fig. 10. Surface-normal density distributions predicted by the baseline and improved models

at station B in Fig. 7 for run 4.

At this point, the reason for the larger separation region predicted by the improved model becomes straightforward. Figure 11 shows that a portion of the flows with a lower degree of dissociation, a higher T_{tr}, and a lower density behind the reattachment shock is redirected into the separation region, which causes an increase in its size while sharing the same mechanisms of the influence of the change in post-shock conditions on the shock standoff distance [10,43].

(a) Baseline model   (b) Improved model
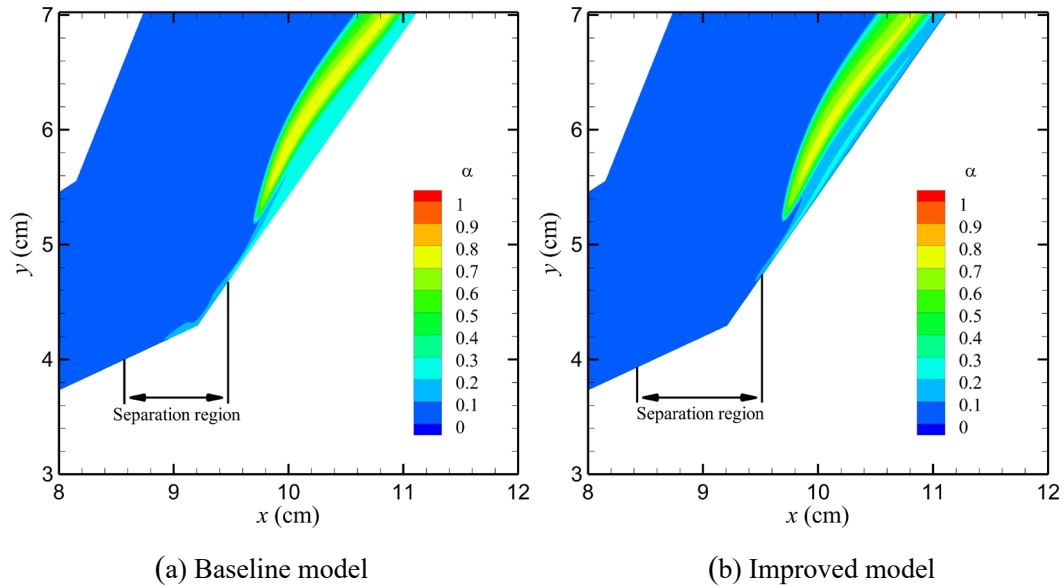
Fig. 11. Contours of degree of dissociation predicted by the baseline and improved models for run 4.

Based on the above analysis, it can be concluded that the inaccurate modeling of vibrational excitation and dissociation in the conventional two-temperature model is indirectly reflected by the sizes of the separation regions, which could be essential to explaining the large discrepancies between numerical results and experimental data for high-enthalpy double-cone flows [17]. Furthermore, one may infer that further inclusion of the non-Boltzmann effects in the improved model would continue to expand the separation region and complete the coupling model between vibrational nonequilibrium and dissociation.

6 Conclusions

Hypersonic thermochemical nonequilibrium flows over a double-cone configuration are numerically simulated with oxygen as the test gas. Two models of oxygen vibrational excitation and dissociation are investigated, including a

conventional two-temperature model and an improved model established based on elementary kinetics. In the conventional two-temperature model, the Landau–Teller model and the Millikan–White expression are used to calculate the energy exchange between the translational mode and the vibrational mode, and the CVDV model is used to account for the vibration–dissociation coupling effects. As for the improved model, the vibrational excitation term, the nonequilibrium dissociation rate coefficients, and the added or removed vibrational energy due to dissociation and recombination are constructed with the kinetic rates of the elementary process involving V–V–T, V–T, and V–D transitions.

The performances of the two models are compared to address the problem of oxygen vibrational excitation and dissociation behind a normal shock under conditions corresponding to a recent shock-tube experiment. The results demonstrate that the two models predict similar post-shock distributions of flow quantities for the case with mild thermochemical nonequilibrium processes; however, for the cases with obvious dissociation, the improved model shows better agreement with the state-specific results and the experimental data, presenting a higher post-shock translational temperature and a lower degree of dissociation.

Three flow conditions selected from the high-enthalpy double-cone experiments conducted at Calspan—University of Buffalo Research Center are simulated; the results indicate that the conventional two-temperature model and improved model yield similar results for the runs with relatively low enthalpies. A remarkable difference can be observed for the condition with total enthalpy greater than 20 MJ/kg. The improved model predicts a larger separation region and a higher peak heat flux than the conventional two-temperature model, with relative differences of 20.3% and 29.2%, respectively. The physics for the difference lies in the inaccurate modeling of vibrational excitation and dissociation by the conventional two-temperature model, which overestimates the degree of dissociation and average density in the separation region. Therefore, a smaller separation bubble is obtained sharing the same effects of the change in post-shock conditions on the shock standoff distance.

It is suggested that the large discrepancies found between numerical results and

experimental data for high-enthalpy double-cone flows in the hypersonic literature can be attributed to the deficiency of the existing vibration–dissociation coupling models. In addition, the model established in this study should be improved to account for non-Boltzmann effects, which is expected to further enlarge the predicted separation region.

Acknowledgements

References

[1] J. J. Bertin, R. M. Cummings, Fifty years of hypersonics: where we've been, where we're going, Progress in Aerospace Sciences, 39 (2003) 511–536.

[2] D. V. Gaitonde, Progress in shock wave/boundary layer interactions, Progress in Aerospace Sciences, 72 (2015) 80–99.

[3] M. S. Holden, T. P. Wadhams, A database of aerothermal measurements in hypersonic flow in "building block" experiments for CFD validation, AIAA 2003–1137, 2003.

[4] M. S. Holden, T. P. Wadhams, Code validation study of laminar shock/boundary layer and shock/shock interactions in hypersonic flow, part A: experimental measurements, AIAA 2001–1031A, 2001.

[5] J. K. Harvey, M. S. Holden, T. P. Wadhams, Code validation study of laminar shock/boundary layer and shock/shock interactions in hypersonic flow, part B: comparison with Navier–Stokes and DSMC solutions, AIAA 2001–1031B, 2001.

[6] M. S. Holden, T. P. Wadhams, M. Maclean, Experimental studies in the LENS supersonic and hypersonic tunnels for hypervelocity vehicle performance and code validation, AIAA 2008–2505, 2008.

[7] I. Nompelis, G. V. Candler, M. MacLean, T. P. Wadhams, M. S. Holden, Numerical investigation of double-cone flow experiments with high-enthalpy effects, AIAA 2010–1283, 2010.

[8] M. S. Holden, T. P. Wadhams, M. Maclean, A. Dufrene, Experimental research and analysis in supersonic and hypervelocity flows in the LENS shock tunnels and expansion tunnel, AIAA 2015–3660, 2015.

[9] M. S. Holden, M. Maclean, T. P. Wadhams, A. Dufrene, Measurements of real gas effects on regions of laminar shock wave/boundary layer interaction in hypervelocity flows for "blind" code validation studies, AIAA 2013–2837, 2013.

[10] H. Shen, C. Y. Wen, Theoretical investigation of shock stand-off distance for non-equilibrium flows over spheres, Chinese Journal of Aeronautics, 31(5) (2018) 990–996.

[11] G. V. Candler, I. Nompelis, M.-C. Druguet, Navier–Stokes predictions of hypersonic double-cone and cylinder-flare flow fields, AIAA 2001–1024, 2001.

[12] D. V. Gaitonde, P. W. Canupp, M. S. Holden, Heat transfer predictions in a laminar hypersonic viscous/inviscid interaction, J. Thermophysics and Heat Transfer, 16(4) (2002) 481–489.

[13] I. Nompelis, G. V. Candler, M. S. Holden, Effect of vibrational nonequilibrium on hypersonic double-cone experiments, AIAA J., 41(11) (2003) 2162–2169.

[14] M.-C. Druguet, G. V. Candler, I. Nompelis, Effect of numerics on Navier–Stokes computations of hypersonic double-cone flows, AIAA J., 43(3) (2005) 616–623.

[15] M.-C. Druguet, G. V. Candler, I. Nompelis, Comparison of physical models in computations of high-enthalpy double-cone flows, AIAA 2006–3419, 2006.

[16] D. Knight, J. Longo, D. Drikakis, D. Gaitonde, A. Lani, I. Nompelis, B. Reimann, L. Walpot, Assessment of CFD capability for prediction of hypersonic shock interactions, Progress in Aerospace Sciences, 48–49 (2012) 8–26.

[17] G. V. Candler, Next-generation CFD for hypersonic and aerothermal flows, AIAA 2015–3048, 2015.

[18] J. Hao, J. Wang, C. Lee, Numerical simulation of high-enthalpy double-cone flows, AIAA J., 55(7) (2017) 2471–2475.

[19] C. Park, Nonequilibrium hypersonic aerothermodynamics, Wiley, New York, 1990.

[20] P. V. Marrone, C. E. Treanor, Chemical relaxation with preferential dissociation

from excited vibrational levels, Physics of Fluids, 6(9) (1963) 1215–1221.

[21] J. Hao, J. Wang, C. Lee, State-specific simulation of oxygen vibrational excitation and dissociation behind a normal shock, Chemical Physics Letters 681 (2017) 69–74.

[22] F. Bonelli, M. Tuttafesta, G. Colonna, L. Cutrone, G. Pascazio, An MPI-CUDA approach for hypersonic flows with detailed state-to-state air kinetics using a GPU cluster, Computer Physics Communications, 219 (2017) 178–195.

[23] K. Sutton, P. A. Gnoffo, Multi-component diffusion with application to computational aerothermodynamics, AIAA 1998–2575, 1998.

[24] R. N. Gupta, J. M. Yos, R. A. Thompson, K. P. Lee, A review of reaction and thermodynamic and transport properties for an 11-species air model for chemical and thermal nonequilibrium calculations to 30 000 K, NASA RP-1232, 1990.

[25] M. J. Wright, D. Bose, G. E. Palmer, Eugene Levin, Recommended collision integrals for transport property computations, part 1: air species, AIAA J., 43(12) (2005) 2558–2564.

[26] J. Hao, J. Wang, C. Lee, Numerical study of hypersonic flows over reentry configurations with different chemical nonequilibrium models, Acta Astronautica, 126 (2016) 1–10.

[27] J. Hao, J. Wang, C. Lee, Development of a Navier–Stokes code for hypersonic nonequilibrium simulations, AIAA 2017–2164, 2017.

[28] R. W. MacCormack, Numerical computation of compressible and viscous flow, AIAA, Reston, 2014.

[29] B. van Leer, Towards the ultimate conservative difference scheme, J. Computational Physics, 32(1) (1979) 101–136.

[30] E. F. Toro, Riemann solvers and numerical methods for fluid dynamics a practical introduction, Springer, Berlin, 1997.

[31] M. J. Wright, G. V. Candler, D. Bose, Data-parallel line relaxation method for the Navier–Stokes equations, AIAA J., 36(9) (1998) 1603–1609.

[32] W. G. Vincenti, C. H. Kruger, Introduction to physical gas dynamics, Krieger, Malabar, 1965.

[33] R. C. Millikan, D. R. White, Systematics of vibrational relaxation, J. Chemical Physics, 39(12) (1963) 3209–3213.

[34] D. Hash, J. Olejniczak, M. Wright, D. Prabhu, M. Pulsonetti, B. Hollis, P. Gnoffo, M. Barnhardt, I. Nompelis, G. Candler, FIRE II calculations for hypersonic nonequilibrium aerothermodynamics code verification: DPLR, LAURA, and US3D, AIAA 2007–0605, 2007.

[35] J. Hao, J. Wang, C. Lee, Assessment of vibration–dissociation coupling models for hypersonic nonequilibrium simulations, Aerospace Science and Technology 67 (2017) 433–442.

[36] D. A. Andrienko, I. D. Boyd, Investigation of oxygen vibrational relaxation by quasi-classical trajectory method, Chemical Physics 459 (2015) 1–13.

[37] M. Lino da Silva, J. Loureiro, V. Guerra, A multiquantum dataset for vibrational excitation and dissociation in high-temperature O_2–O_2 collisions, Chemical Physics Letters, 531 (2012) 28–33.

[38] D. A. Andrienko, I. D. Boyd, Master equation study of vibrational and rotational relaxations of oxygen, J. Thermophysics and Heat Transfer, 30(3) (2016) 533–552.

[39] D. A. Andrienko, K. Neitzel, I. D. Boyd, Vibrational relaxation and dissociation of oxygen in molecule-atom mixtures, AIAA 2015–3251, 2015.

[40] L. B. Ibraguimova, A. L. Sergievskaya, V. Yu. Levashov, O. P. Shatalov, Yu. V. Tunik, I. E. Zabelinskii, Investigation of oxygen dissociation and vibrational relaxation at temperatures 4000–10800 K, J. Chemical Physics, 139 (2013) 034317.

[41] M.-C. Druguet, G. V. Candler, I. Nompelis, Effect of numerics on Navier–Stokes computations of hypersonic double-cone flows, AIAA J., 43(3) (2005) 616–623.

[42] B. E. Edney, Effects of shock impingement on the heat transfer around blunt bodies, AIAA J., 6(1) (1968) 15–21.

[43] H. Babinsky, J. K. Harvey, Shock wave–boundary-layer interactions, Cambridge University Press, New York, 2011.